Supplementary Information

A high-energy asynchronously reverse dual-ion battery based on H^-/Na^+ insertion chemistry

Author Information

Wen Luo,*[a] Xiangchen Zhang,[b] Hongwei Cai,[b] Houde Xu,[b] Ruixi Chen,[b] Jean-Jacques Gaumet [bc] and Kai Fu *[ab]

School of Physics and Mechanics, Wuhan University of Technology, Wuhan 430070, P. R. China. E-mail: luowen_1991@whut.edu.cn, kaifu@whut.edu.cn

State Key Laboratory of Advanced Technology for Materials Synthesis and Processing, Wuhan University of Technology, Wuhan 430070, P. R. China.

Laboratoire de Chimie et Physique: Approche Multi-échelles, des Milieux Complexes (LCP-A2MC), Institut Jean Barriol, Université de Lorraine, Metz 57070, France.

Experimental Section

***Chemicals and Materials*:** $MnSO_4 \cdot H_2O$, $(NH_4)_2S_2O_8$, NaCl, tetramethylammonium hydroxide (TMAOH) and NaOH were purchased from Aladdin Co., Ltd. Graphene was purchased from Nanjing XFNANO Materials Tech Co., Ltd. Polyurethane resin dissolved in aromatic solvents and superfine graphite were purchased from Dawu YueHua protective products Co., Ltd. Mg–Y bimetallic alloy target was purchased from Shijiazhuang Huake metal material technology Co., LTD. Pd target was purchased from ZhongNuo Advanced Material (Beijing) Technology Co., Ltd.

Preparation of γ-MnO_2 powders: γ-MnO_2 powders were synthesized via hydrothermal methods. Typically, 3.375 g of $MnSO_4 \cdot H_2O$ was first dissolved in 80 mL DI water, and 4.575 g of $(NH_4)_2S_2O_8$ was added to the solution. After stirring for 30 min, the mixture solution was transferred to a 100 mL autoclave and then heated at 90 °C for 24 h. After cooling to room temperature, the solid precipitates were collected after centrifuging and washing with DI water eight times to remove the residual salts. The powder was dried overnight at 80 °C.

***Preparation of cathode ink and current collector inks*:** The above-prepared γ-MnO_2 powders (40 wt%), Graphene (20 wt%), superfine graphite (10 wt%), acetylene black (10 wt%) were uniformly mixed with polyurethane resin (20 wt%) dissolved in aromatic solvent and then stirring for 30 min. Gel-like cathode ink was obtained. The current collector ink was prepared using the same regime except that the reagent proportion was Graphene (60 wt%), superfine graphite (10 wt%), acetylene black (10 wt%) and polyurethane resin (20 wt%).

Preparation of planar batteries: The micro-batteries with designed patterns and dimensions could be easily integrated on flexible substrates in four steps by combining screen printing and magnetron sputtering techniques. Initially, conductive graphene ink was printed onto polyethylene terephthalate (PET) substrates by a screen-printed process to fabricate current collectors with pre-designed planar patterns such as interdigital microelectrodes. Then, Mg-Y alloy thin films with Pd interlayers were deposited on the anodic four fingers through direct current magnetron sputtering technique at room temperature in high purity argon (99.999%) of 0.6 Pa. A thin Pd capping layer of ~20 nm was deposited on top and between 500 nm of Mg-Y alloy films to prevent the anode films from oxidation and to catalyze

hydrogenation/dehydrogenation. Thirdly, the cathode ink containing 40 wt% of γ-MnO_2 was homogeneously mixed and, after that, printed on the cathodic four fingers of the above-fabricated graphene current collectors and dried in a vacuum oven at 80 °C for 12 h. Finally, planar ARDIBs were packaged with polyimide polymer tape coating after adding an aqueous electrolyte onto the projected finger areas. The dose of electrolyte for a full battery was 35 μL cm^{-2}. The pattern and dimension of the planar battery can be adjusted by replacing the screen mesh.

***Material and electrode characterization*:** The crystallographic structures of the samples were characterized by X-ray diffraction (XRD) using the Bruker AXS GmbH with a Cu Kα X-ray source (λ=1.5406 Å). The scanning electron microscopy (SEM) morphology and composition of the electrode materials were characterized by a JEOL-7100F microscope with an energy dispersive spectrometer (EDS) assistant. To investigate the morphological evolution, ex-situ SEM images were acquired from electrodes harvested at different cycle intervals (pristine, 5, 20, 50, 100, and 200 cycles) after washing with deionized water. Scanning transmission electron microscopy with energy–dispersive X-ray spectroscopy (STEM–EDS) mappings were conducted on a Talos F200S (Thermo Scientific) to reveal the intrinsic lattice structure and elemental distribution. For STEM–EDS observations, the cycled electrodes were ultrasonically dispersed in ethanol to remove surface residues. The thin films were directly deposited on Si wafers or TEM grids for SEM and TEM measurements. The TOF-SIMS spectrometry was performed on a PHI nano TOFII Time-of-Flight SIMS instrument. An atomic force microscopy (AFM) map was obtained using SmartSPM (HORIBA). XPS data were collected on an ESCALAB250Xi photoelectron spectrometer (Thermo Fisher Scientific), with all binding energies referenced to the C 1s peak (284.8 eV). Raman spectroscopy was performed using a HORIBA Raman microscope with a 532 nm laser. A customized in-situ cell with an optical window was employed to detect the formation of Pd–H bonds during electrochemical polarization.

Electrochemical measurements: GCD and EIS tests were conducted on a CHI760E electrochemistry workstation (Shanghai Chenhua Instrument Co., Ltd., Shanghai, China). Cycle stability tests were performed on the LAND battery test system (CT3001A, Wuhan, China) and Neware battery test system (CT-4008, Shenzhen, China) at 20 °C. The half battery was assembled in a PTFE Swagelok-type three-electrode system, in which a Hg/HgO electrode served as the reference electrode. In this work, all

potential values are converted into values versus standard hydrogen electrodes (SHE). Full batteries were tested using stainless steel holding pins to connect Graphene current collectors with the external circuit linked to the battery test system or electrochemical workstation.

Note S1: Detailed electrochemical mechanism and closed circuit of H^-–Na^+ ARDIB

In this note, 'cathode/anode' refer to the MnO_2 electrode and Mg-Y electrode, respectively; during charging/discharging their electrochemical roles (oxidation/reduction) interchange. To clarify the charge storage mechanism and the completion of the closed circuit in the H^-–Na^+ ARDIB, the detailed electrochemical half-reactions and the ionic balance process are described below.

(1) Charging process

During the charging process, the system operates as follows to store energy:

Electron flow (external circuit). Driven by an external power source, electrons (e^-) flow from the MnO_2 cathode through the external circuit to the Mg-Y anode.

Cathode reaction (oxidation + cation release). At the cathode, the sodium-intercalated manganese oxide (Na_xMnO_2) undergoes oxidation. This process extracts Na^+ ions from the host structure and releases them into the aqueous electrolyte. The half-reaction can be expressed as:

$$Na_xMnO_2 \overset{Charge}{\rightarrow} Na_{x-\delta}MnO_2 + \delta Na^+ + \delta e^-$$

Anode reaction (reduction + anion storage via in-situ conversion). At the anode, electrons reduce water molecules on the catalytic Pd surface. Crucially, free H^- ions do not migrate from the electrolyte. Instead, H_2O molecules are adsorbed and dissociated; the hydrogen species are reduced in-situ to form H^- anions, which immediately diffuse into the Mg-Y lattice to form metal hydrides. Simultaneously, OH^- ions are released into the electrolyte. The half-reaction can be expressed as:

$$Mg-Y + \delta H_2O + \delta e^- \overset{\substack{Charge \\ Pd\ catalyst}}{\rightarrow} Mg-Y-H_\delta + \delta OH^-$$

Stepwise anode reaction can be expressed as:

Step1: $H_2O \longrightarrow H^+ + OH^-$

Step2: $H^+ + e^- \longrightarrow H_{ads} (Volmer\ step\ on\ Pd)$

Step3: $H_{ads} + e^- \longrightarrow H^- (embedded)$

Step4: $Mg-Y + H^- \longrightarrow Mg-Y-H\ (H^-\ insertion\ and\ storage)$

Ionic flux and closed circuit. The electrolyte receives Na^+ from the cathode and OH^- from the anode. These ions diffuse into the bulk solution to maintain local and global electroneutrality. This concurrent release of cations and anions satisfies the condition for a closed ionic circuit without

requiring the thermodynamically impossible migration of H^- through the aqueous medium.

(2) Discharging process

During the discharging process, the stored chemical energy is converted back into electrical energy:

Electron flow (external circuit). Electrons flow from the Mg-Y anode through the external load to the MnO_2 cathode.

Anode reaction (oxidation + anion release/water regeneration). The metal hydrides (Mg-Y-H) are oxidized, releasing stored H^- which react with OH^- ions at the interface to regenerate H_2O molecules and release electrons. The half-reaction can be expressed as:

$$Mg-Y-H_\delta + \delta OH^- \xrightarrow[Pd\ catalyst]{Discharge} Mg-Y + \delta H_2O + \delta e^-$$

Cathode reaction (reduction + cation insertion). The MnO_2 cathode accepts electrons and captures Na^+ ions from the electrolyte. The half-reaction can be expressed as:

$$Na_{x-\delta}MnO_2 + \delta Na^+ + \delta e^- \xrightarrow{Discharge} Na_xMnO_2$$

Ionic Flux and Closed Circuit: The continuous consumption of OH^- at the anode and Na^+ at the cathode leads to a decrease in the bulk electrolyte concentration. The ionic balance is maintained by the diffusion of ions from the bulk solution to the electrode interfaces, closing the circuit.

(3) Electrochemical consistency

This mechanism explicitly demonstrates that the ARDIB configuration strictly adheres to fundamental electrochemical principles:

No violation of ion migration direction: Na^+ and OH^- move in opposite directions when necessary to balance local charge, consistent with electric field effects in electrolyte.

H^- does not migrate in bulk: It is generated and consumed at the anode/electrolyte interface, avoiding any contradiction with anion transport conventions.

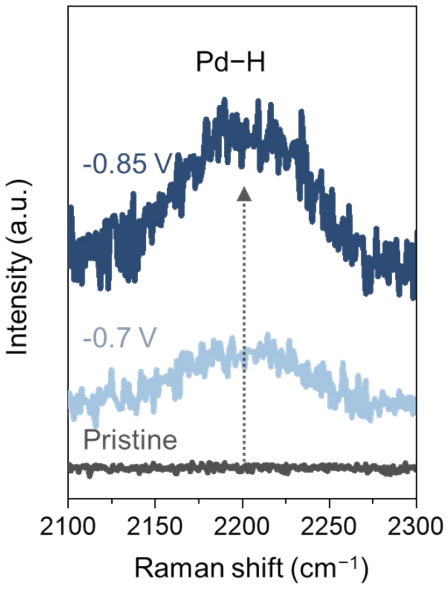

Figure S1 In situ Raman spectra of Pd-capped Mg-Y alloy anode.

The band at ~2200 cm^{-1}, assigned to Pd–H stretching vibrations, progressively intensifies upon cathodic polarization. This result distinctly detects the emergence of Pd–H vibration signals during the charging process, verifying the intermediate catalytic pathway of hydrogen species.

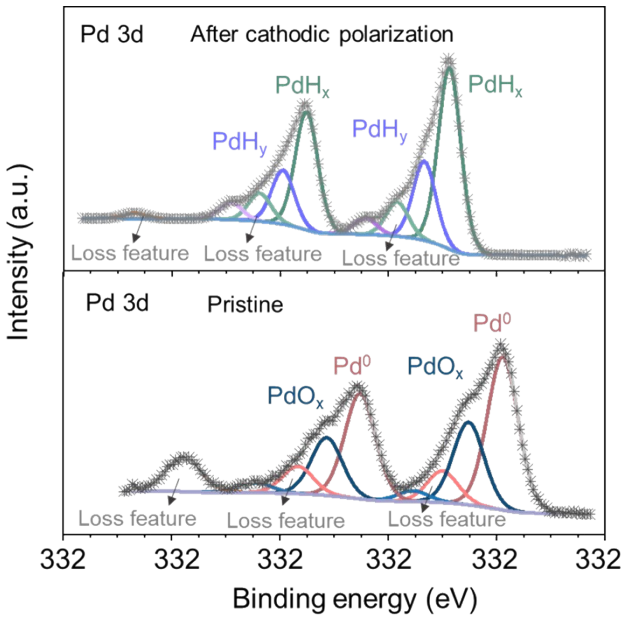

Figure S2 XPS spectra of Pd 3d for the pristine and cycled anodes. Upon cathodic polarization (under strong reducing potentials), the spectra reveal an increase in the valence state of Pd. This indicates that Pd is oxidized, accompanied by the reduction of hydrogen to H^-, resulting in the formation of palladium hydrides.

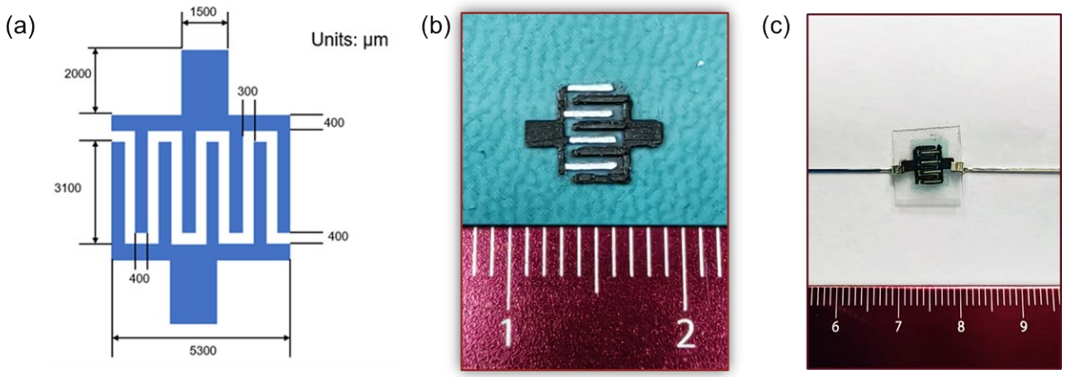

Figure S3 The designed projection and digital photographs of the micro-battery. (a) The projection and size parameters of a micro-battery. (b) Digital photographs of a micro-battery. (c) Digital photographs of a micro-battery after electrochemical tests.

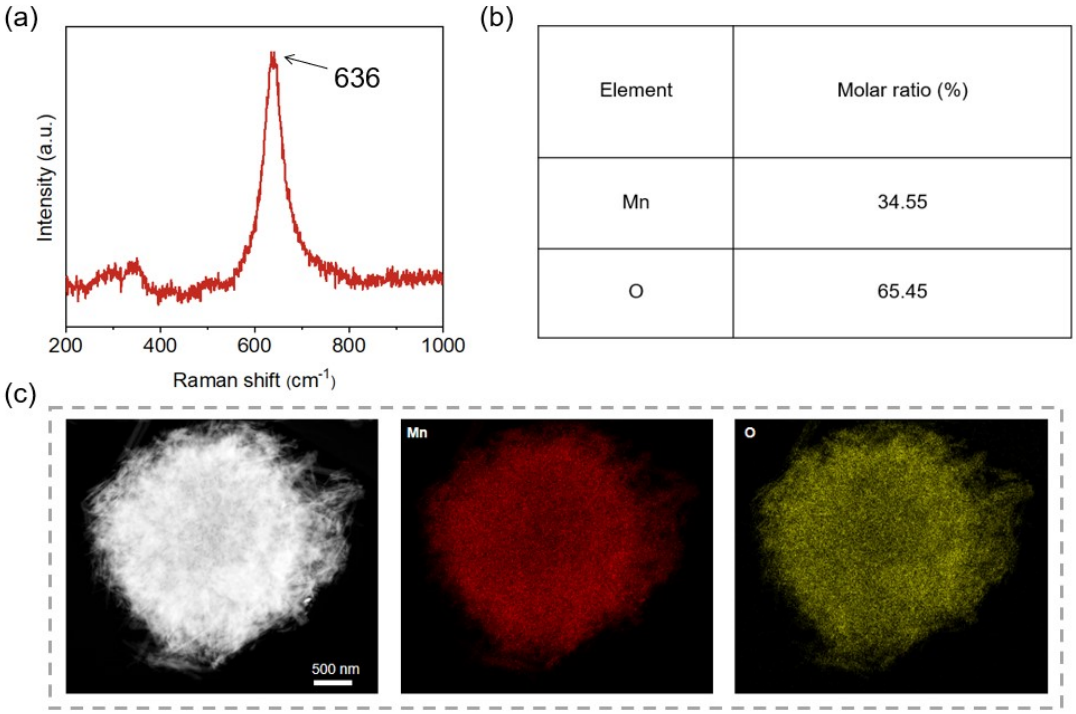

Figure S4 Characterization for the γ-MnO_2 particles. (a) Raman spectra of MnO_2 sample. The peaks 636 cm^{-1} demonstrate characteristic of γ-MnO_2 phase[1]. (b) Element composition derived by inductively coupled plasma-atomic emission spectrometry (ICP) and CHNS/O organic element analyses. (c) TEM image and EDS mapping of a γ-MnO_2 particle. Uniform distribution of Mn and O elements was shown in the γ-MnO_2 particle.

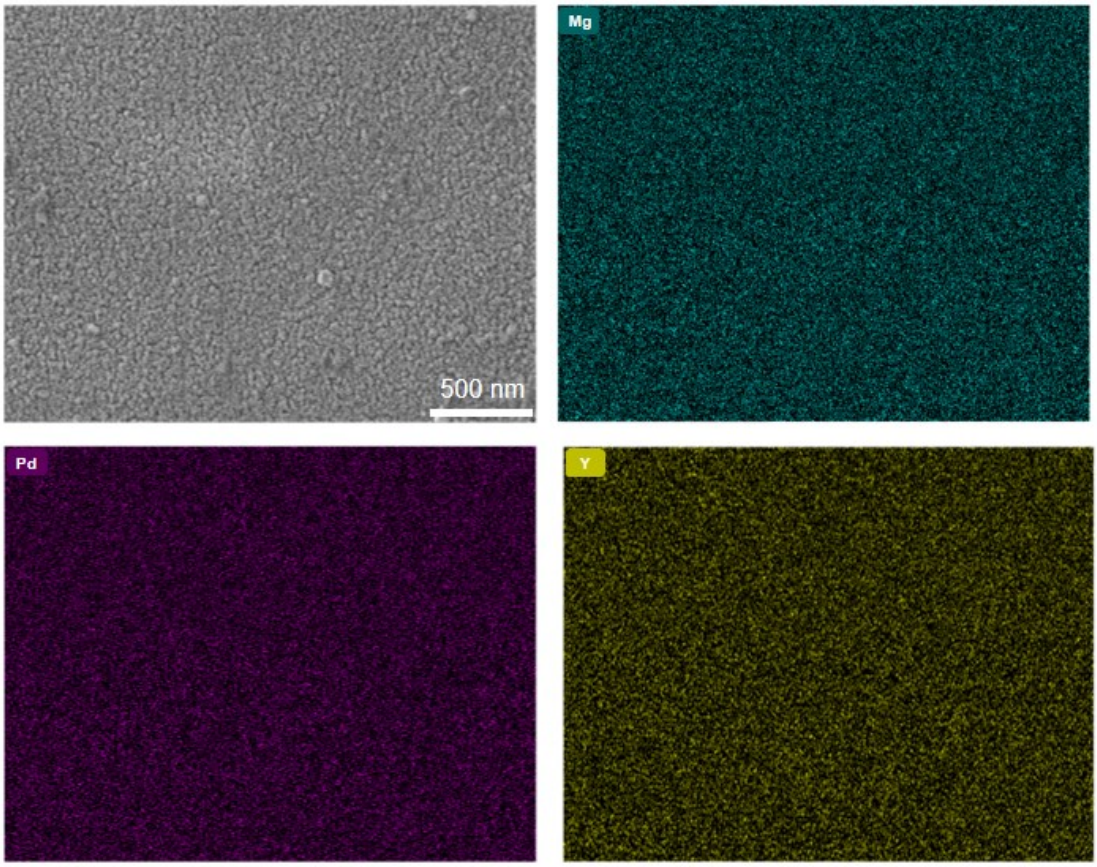

Figure S5 SEM image and EDS mapping of the Pd capped Mg-Y alloy anode. The SEM image of the top view of the anode shows the uniform distribution of the tiny nanograins. Uniform distribution of Mg, Y and Pd elements was shown in the anode.

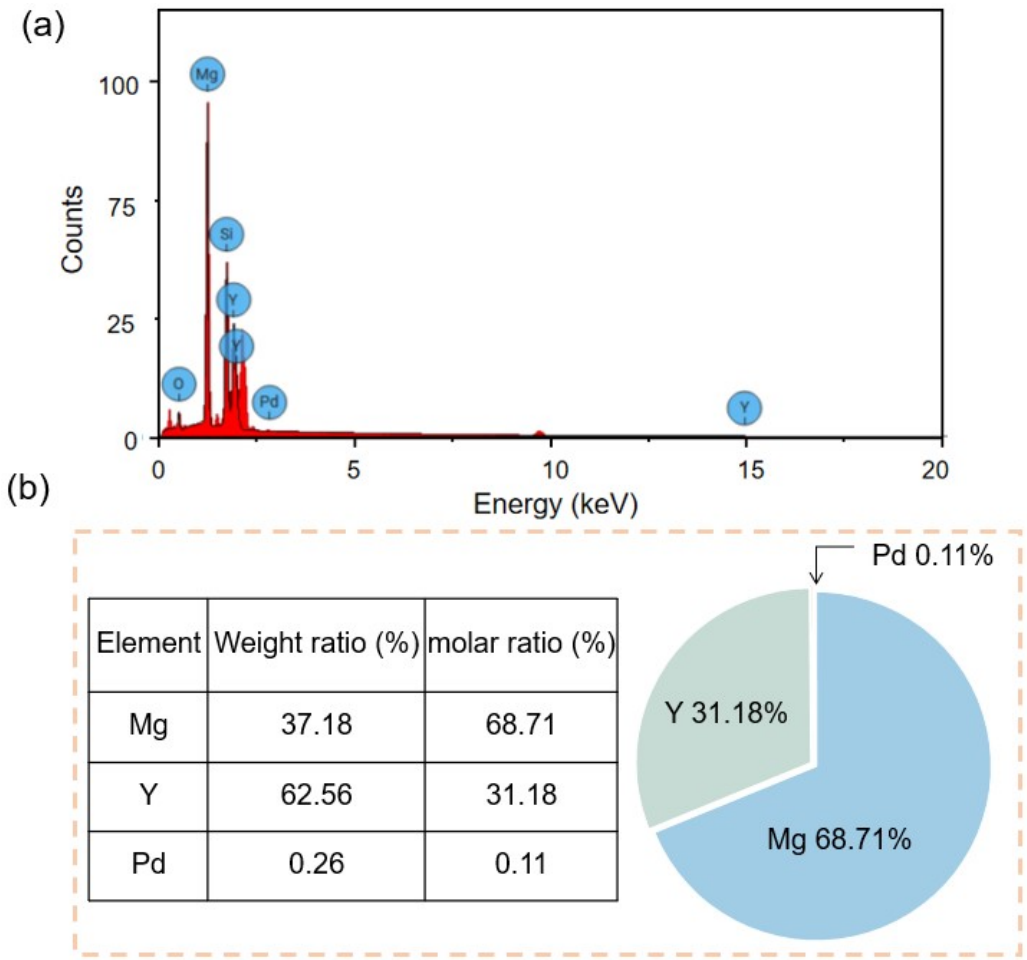

Figure S6 STEM–EDS analyses of Pd capped Mg-Y alloy anode. (a) EDS spectra of anode. The Si and O signals can be ascribed to the SiO_2 species on the surface of monocrystalline silicon substrate. (b) The elements proportion of anode. The Mg/Y atomic ratio is 2.2, which is basically consistent with the atomic ratio of $Mg_{24}Y_5$ phase.

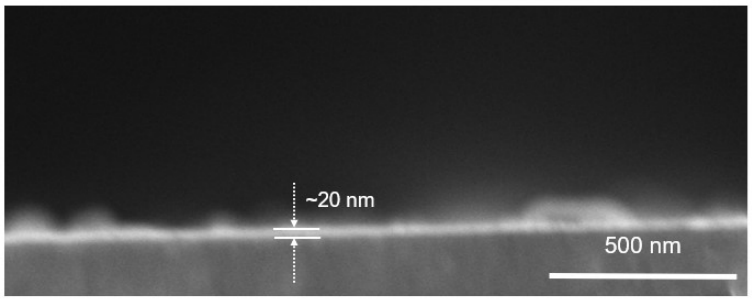

Figure S7 The SEM image of the cross-section view of the anode. The Pd layer was approximately 20 nm.

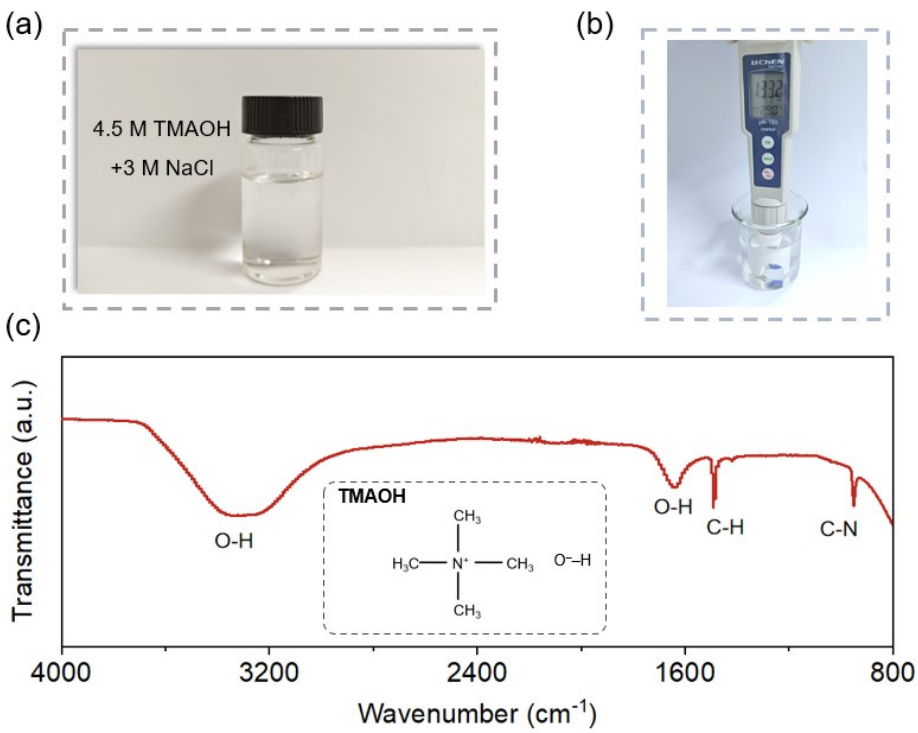

Figure S8 Characterization for 4.5 M TMAOH+3 M NaCl aqueous electrolyte. (a) Optical photographs of 4.5 M TMAOH+3 M NaCl electrolyte. (b) The pH test. The 4.5 M TMAOH+3 M NaCl electrolyte delivers a suitable alkaline environment (pH value of ~13). (c) FTIR spectrum. The vibration band at 3332cm^{-1} and 1641 cm^{-1} is attributed to the stretching of O–H group, the peak at 1490 cm^{-1} is attributed to the in-plane bending vibration of C–H group, and the peak at 950 cm^{-1} is attributed to the stretching vibration of C-N group.

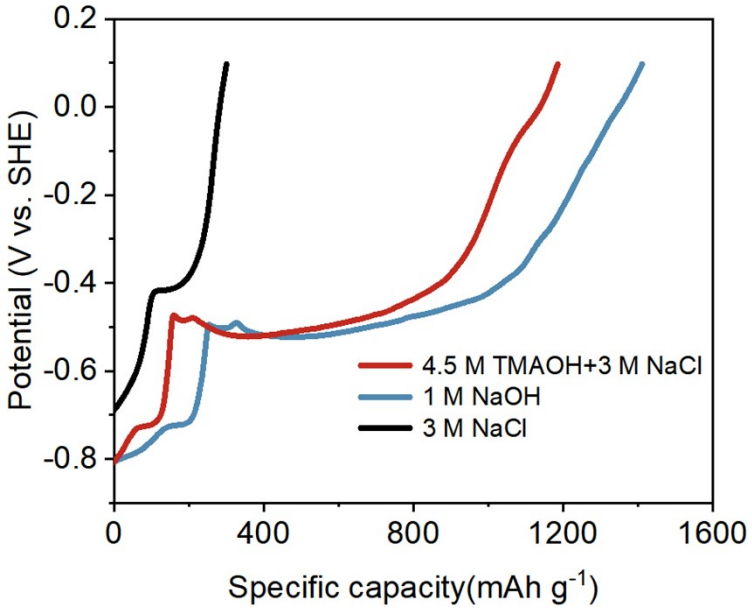

Figure S9 Charge/discharge curves of the Pd capped Mg-Y alloy anode in different electrolytes at current density of 4 mA cm^{-2}.

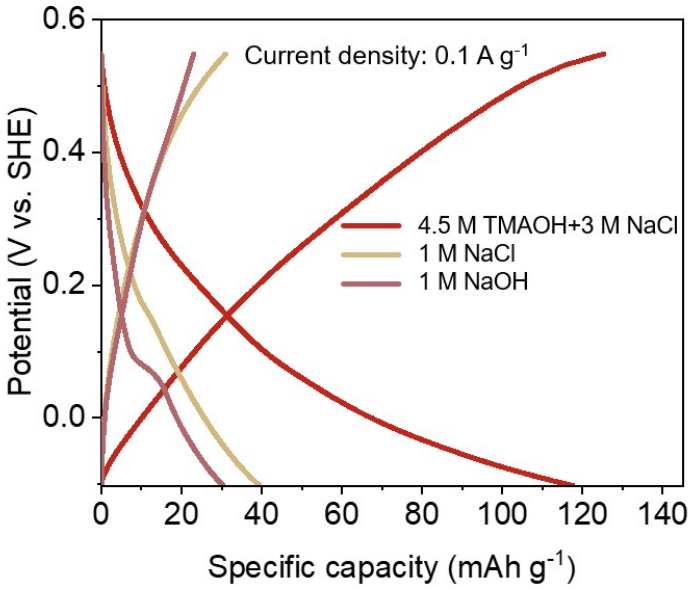

Figure S10 Charge/discharge curves of γ-MnO_2 cathode in different electrolytes at current density of 0.1 A g^{-1}.

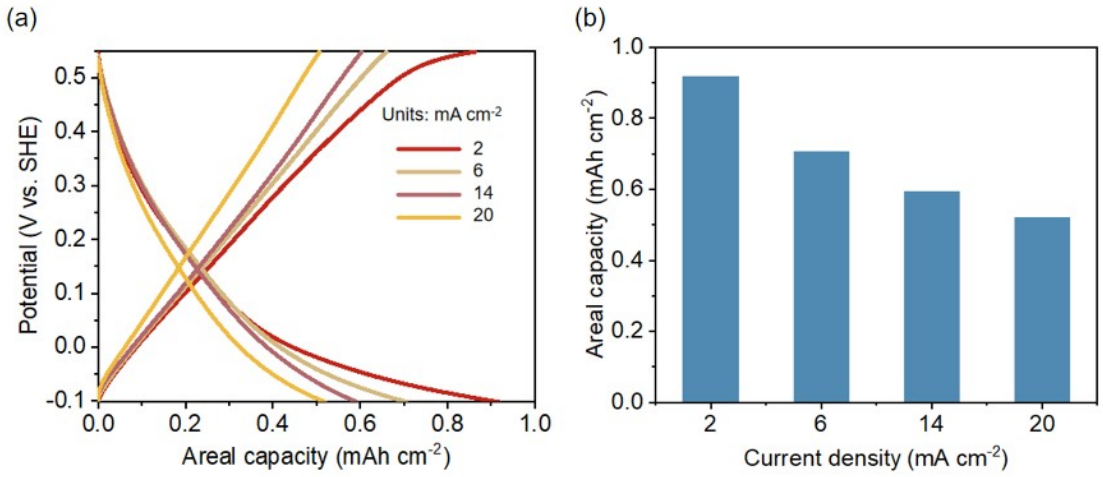

Figure S11 Rate capability of γ-MnO_2 micro-cathode. (a) Galvanostatic charge/discharge curves of γ-MnO_2 cathode at different current densities. (b) Areal capacities of γ-MnO_2 cathode at different current densities.

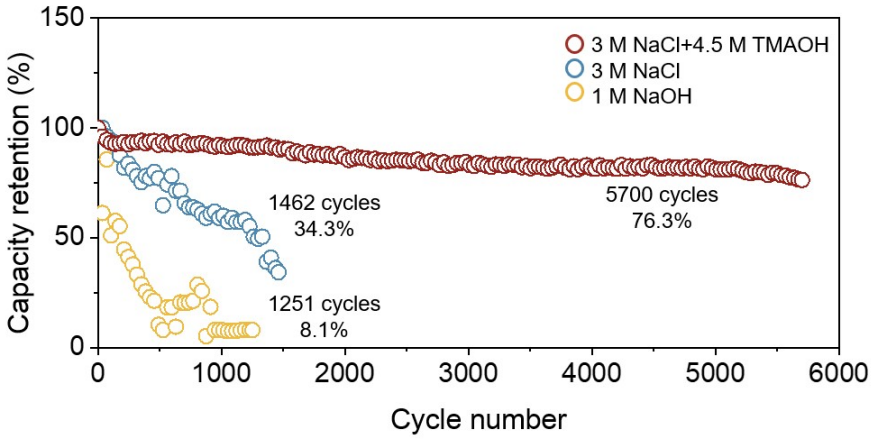

Figure S12 Cycle performance of H^{-}–Na^{+} ARDIB in different electrolytes at current density of 10 mA cm^{-2}. The ARDIB exhibits a long lifespan of >5700 cycles with a high capacity retention of 76.3% in the 4.5 M TMAOH+3 M NaCl electrolyte. In contrast, the ARDIBs demonstrate poor cycling performance and failure in 1500 cycles in NaOH and NaCl electrolytes.

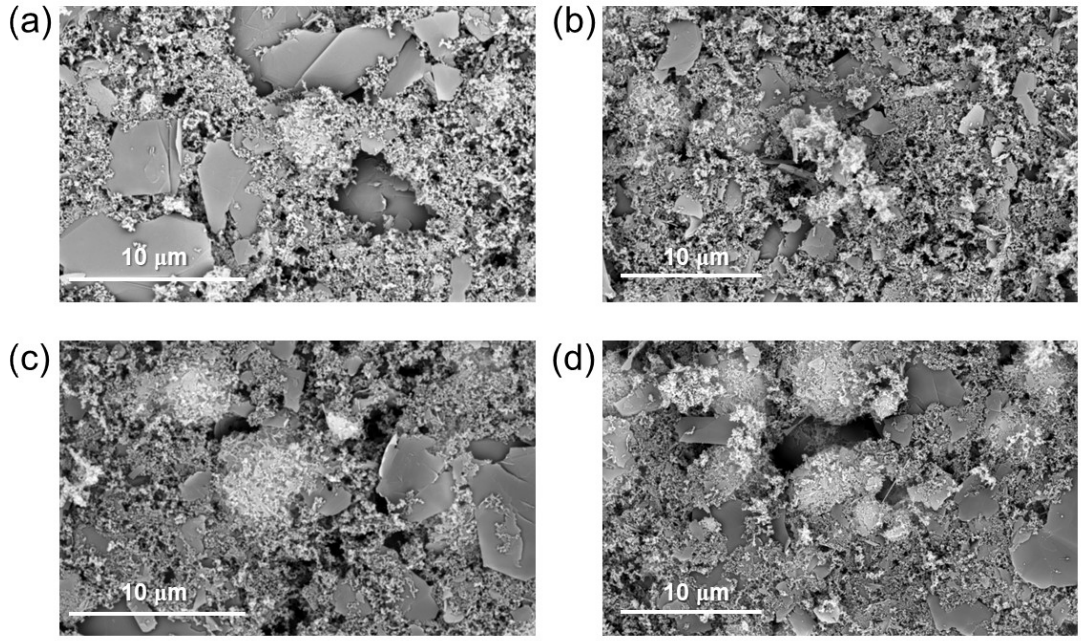

Figure S13 Assessing the morphological representativeness of the MnO_2 cathode after 100 cycles. (a–d) SEM micrographs acquired from four distinct, randomly selected regions of the same electrode. Additional SEM images confirming the representativeness of Fig. 4a (different particles/regions). The qualitative consistency observed across these diverse locations confirms that the reported structural reconstruction is a general and homogeneous phenomenon throughout the electrode surface, rather than an isolated local event.

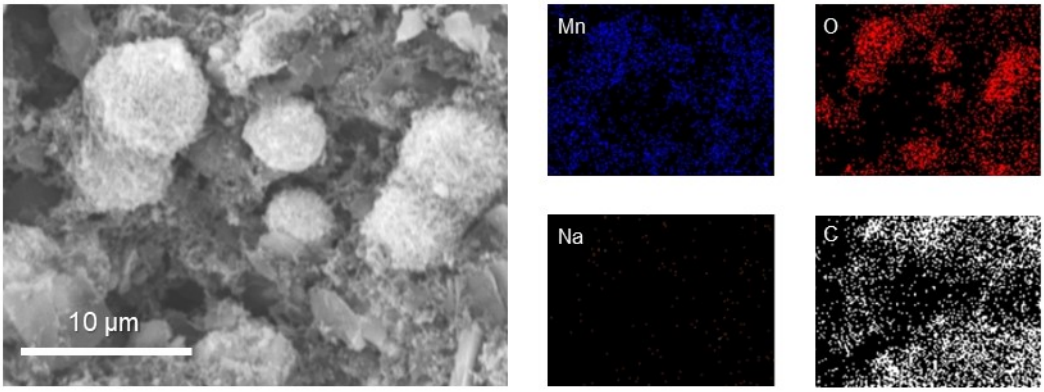

Figure S14 SEM–EDS elemental mapping of the pristine MnO_2 cathode (before cycling). The Na signal is negligible in the pristine state, establishing a baseline and confirming that Na detected after cycling originates from electrochemical insertion rather than pre-existing contamination or sample handling.

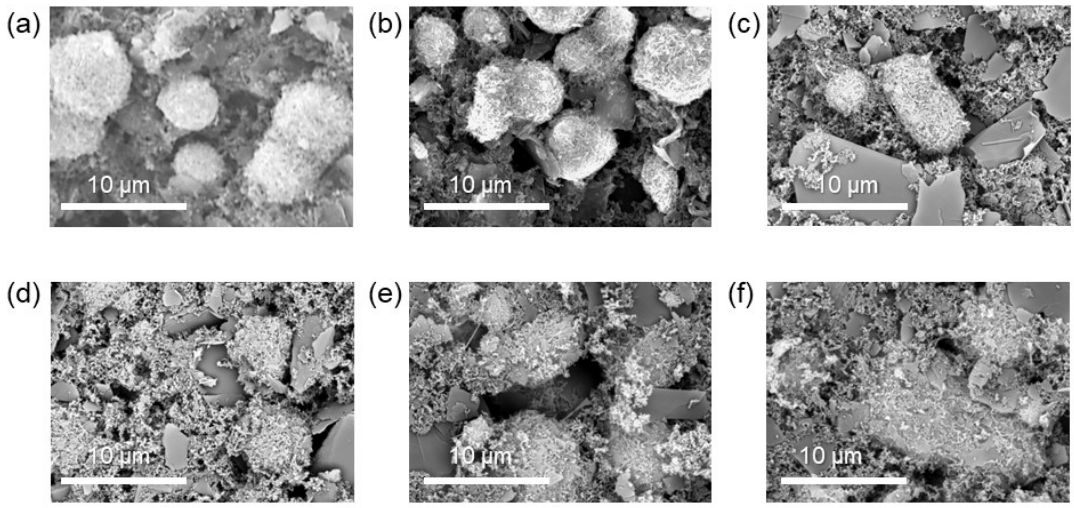

Figure S15 Representative SEM images of the MnO_2 cathode collected at different cycle numbers. (a) pristine, (b) 5, (c) 20, (d) 50, (e) 100, and (f) 200 cycles.

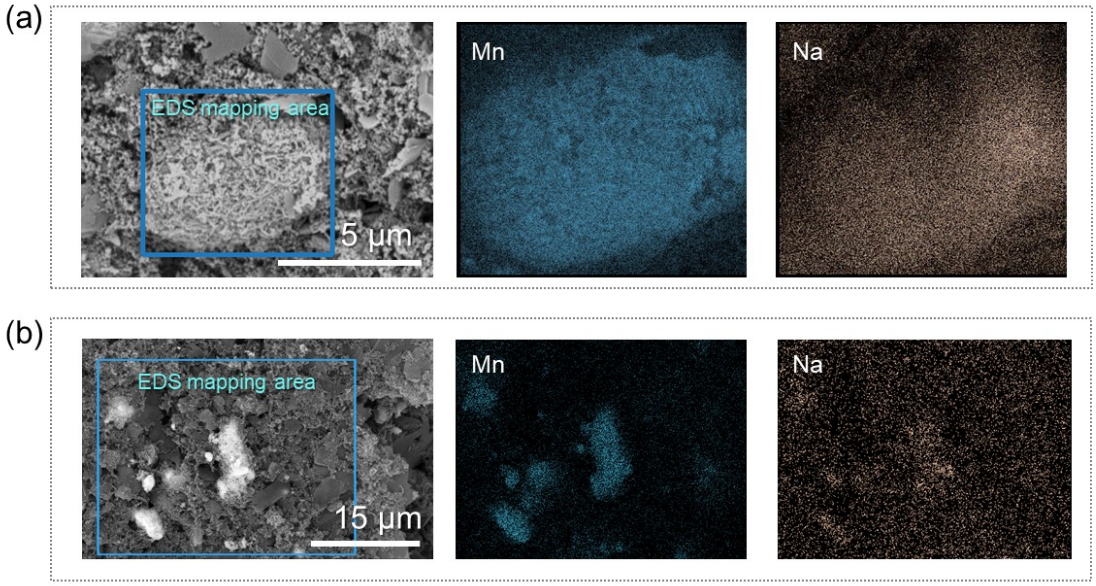

Figure S16 Multi-scale SEM–EDS analysis of the MnO_2 cathode after 100 cycles. (a) and (b) represent distinct regions of the same electrode captured at different magnifications, illustrating the spatial distribution of Na.

While a general Na distribution is observed, certain regions (as seen in these representative scans) exhibit localized high-intensity signals or apparent nonuniformity. These inconsistencies are attributed to the inherent surface roughness of the porous electrode, variations in particle thickness, and potential interference from the carbon binder or trace residual electrolyte. This suggests that SEM–EDS alone reflects surface-dominated signals and may not definitively represent the intrinsic lattice-level homogeneity.

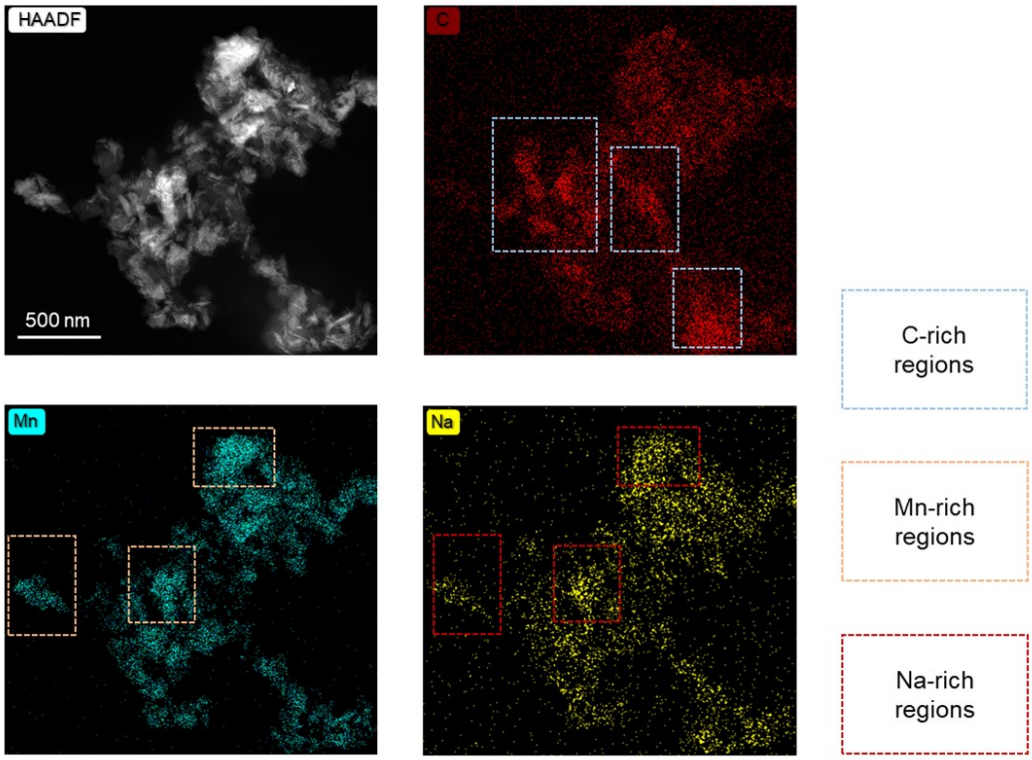

Figure S17 STEM–EDS mapping of the 100-cycle MnO_2 cathode (intrinsic Na distribution after cleaning).

The sample was prepared via ultrasonic dispersion to remove surface residues. The results show that the Na distribution is highly uniform and spatially correlated with the Mn signal (active material) rather than the carbon support. This confirms homogeneous Na^+ intercalation into the lattice and rules out the formation of irreversible agglomerates.

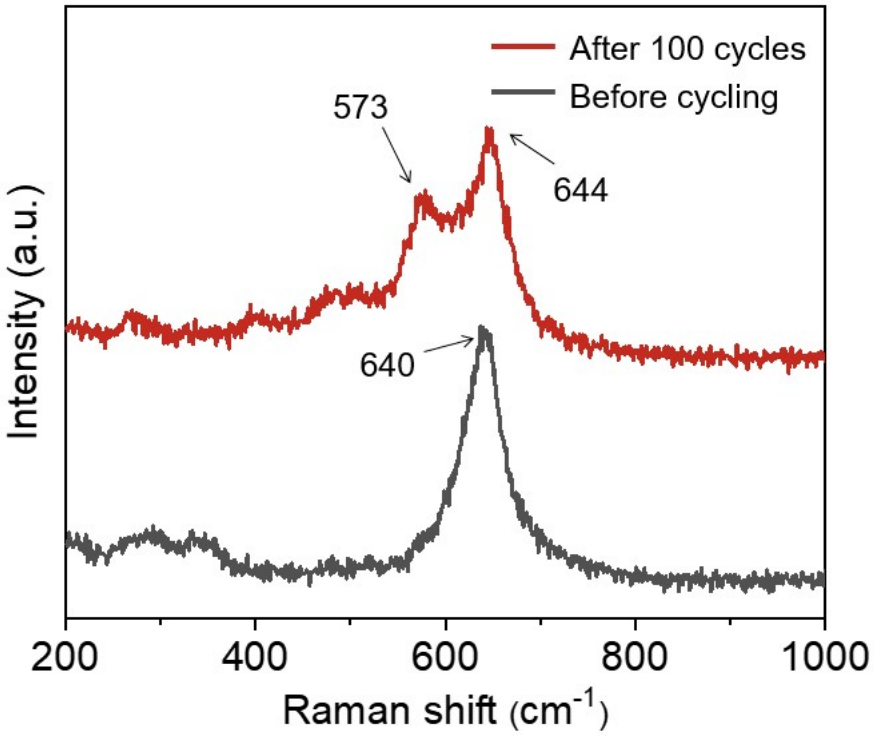

Figure S18 Raman spectra of pristine cathode and cathode after 100 cycles. The peak at about 573 cm^{-1} was definitely deformation modes of Mn-O-Mn chain in δ-MnO_2 octahedral lattice, and the strong peak at about 640 cm^{-1} was interpreted as Mn-O stretching modes in γ-MnO_2.[1] The new Raman peak at 573 cm^{-1} appeared after 100 cycles, indicating the formation of δ-MnO_2 phase.[2]

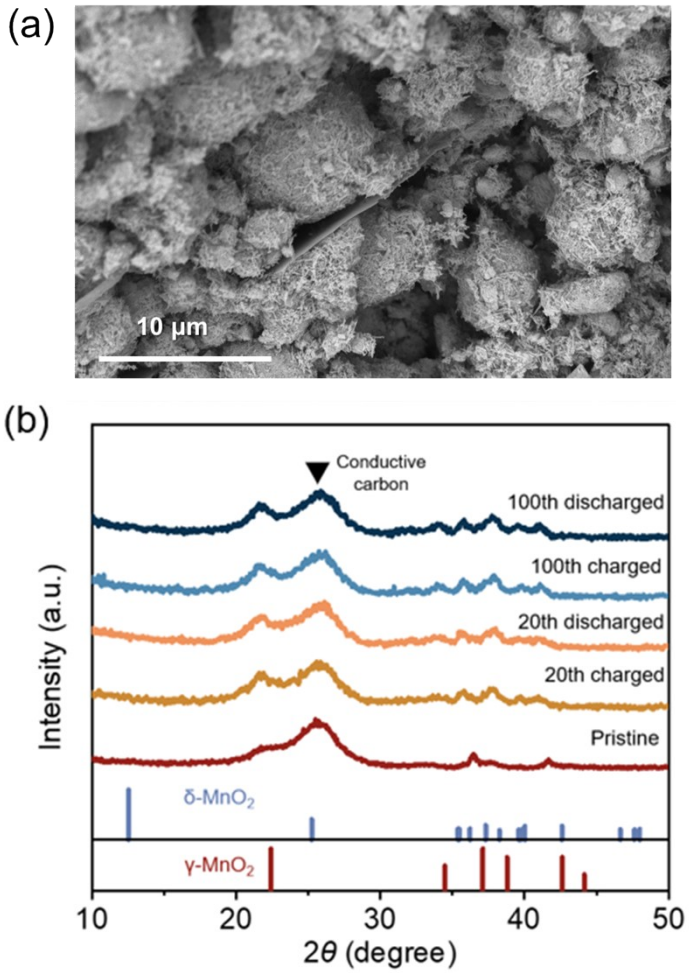

Figure S19 Structural and morphological characteristic of MnO_2 cathode after 100th cycles in 3 M NaCl aqueous electrolyte. (a) SEM image of the MnO_2 cathode. The MnO_2 particles maintain their sphere-like hierarchical structure. (b) The ex-situ XRD patterns of cathode during cycles. No peak intensities at 12.4° can be observed after 100 cycles. In situ structural evolution of cathode was absent in NaCl aqueous electrolyte without TMAOH additives.

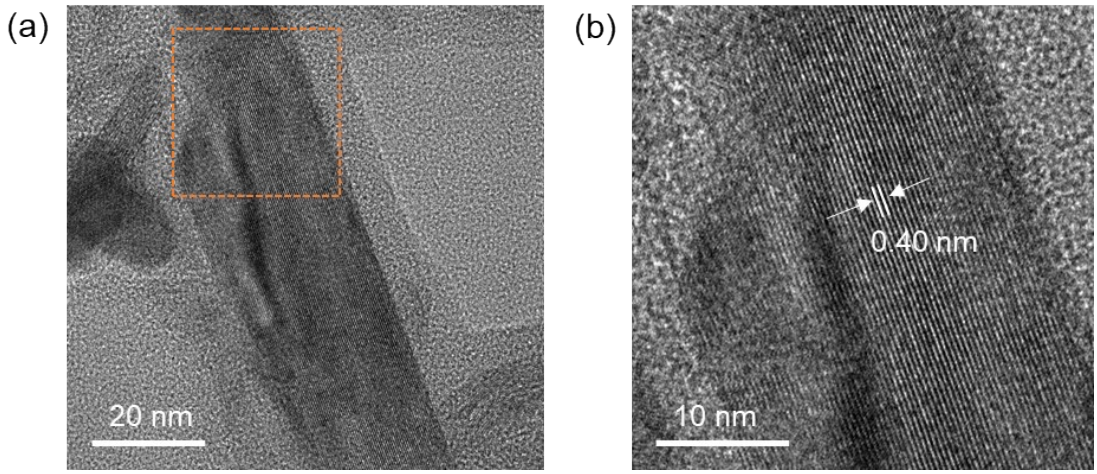

Figure S20 TEM images of MnO_2 cathode cycled in 3 M NaCl aqueous electrolyte. (a) Low-magnification TEM image of a MnO_2 nanosheet. (b) The high-resolution TEM image of the dashed box region in (a). No obvious expansion of interlayer spacing can be observed in the scratched sample from the MnO_2 electrode with 100 cycles in 3 M NaCl aqueous electrolyte without TMAOH additives.

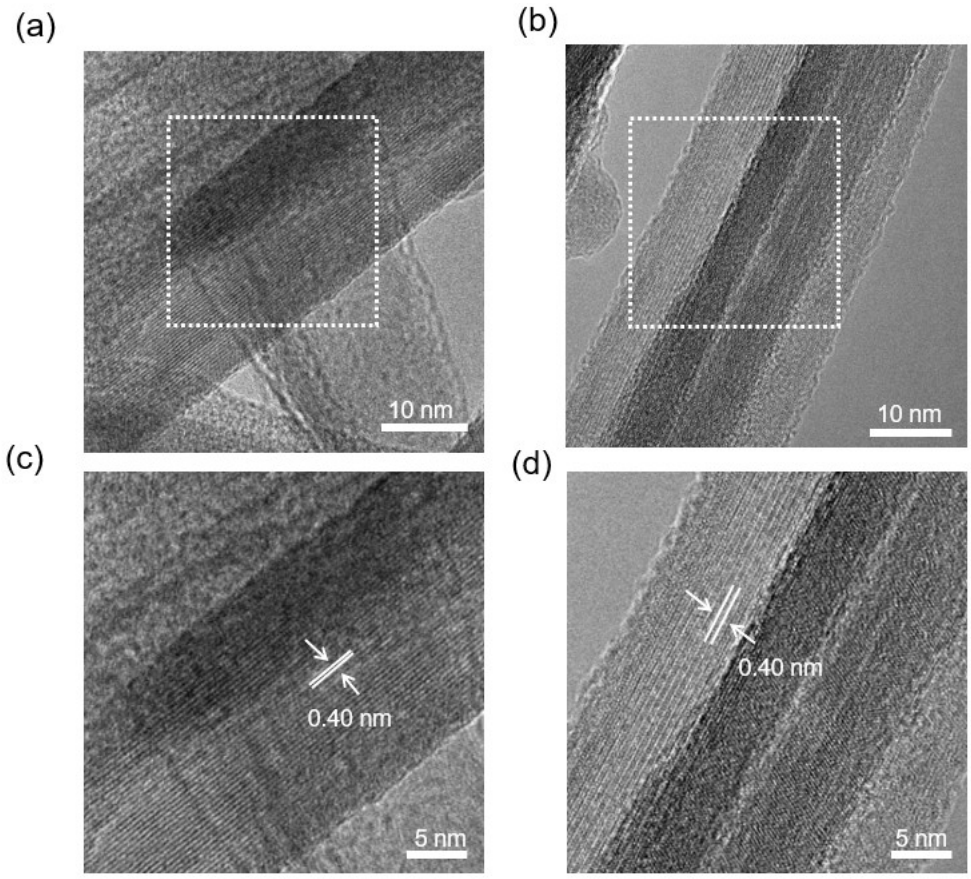

Figure S21 HRTEM images of scratched sample from the pristine MnO_2 electrode. (a, b) Two selected areas of MnO_2 nanosheets. (c, d) The high-resolution TEM images of the dashed box region in (a) and (b), respectively. The HRTEM image perpendicular to the (101) crystal plane, proving that the interlayer spacing is 0.40 nm before cycling.

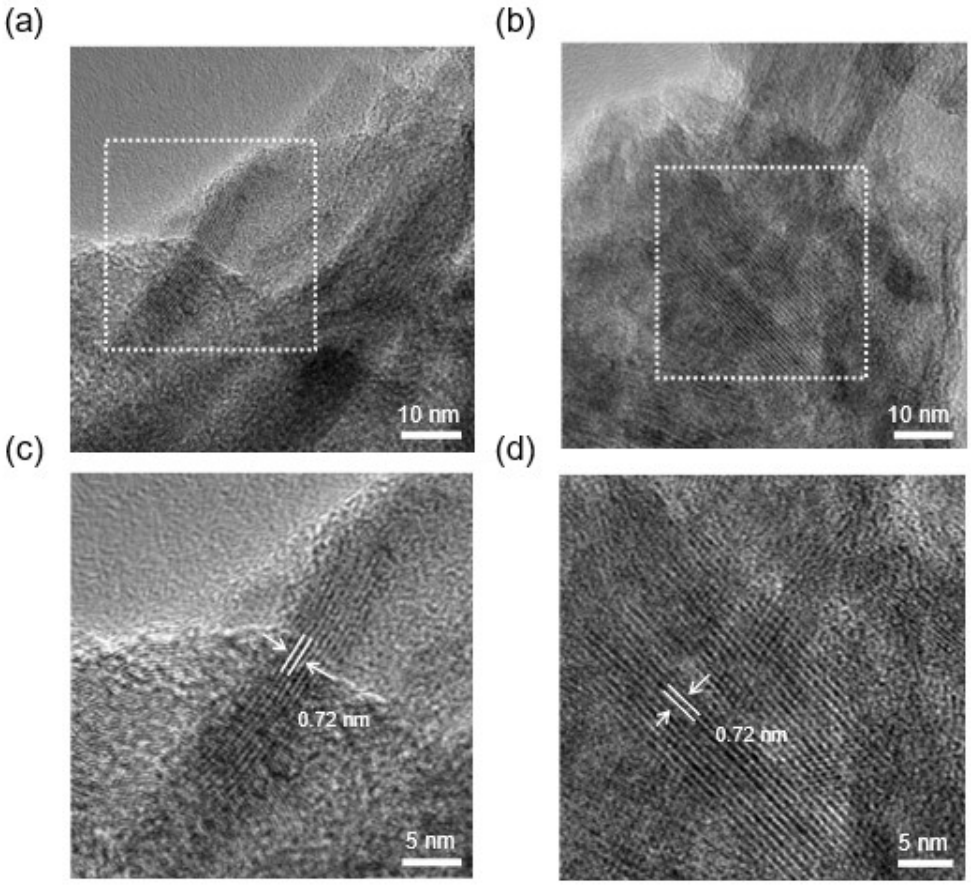

Figure S22 HRTEM images of scratched sample from the MnO_2 electrode with 100 cycles in the 4.5 M TMAOH+3 M NaCl electrolyte. (a, b) Two selected areas of MnO_2 nanosheets. (c,d) The high-resolution TEM images of the dashed box region in (a) and (b), respectively. The HRTEM image perpendicular to the (101) crystal plane, proving that the interlayer spacing is 0.40 nm before cycling. The interlayer spacing of the scratched sample from the MnO_2 electrode expanded to 7.1 Å after 100 cycles. The insertion of large-sized TMA^+ leads to interlayer expansion, which promotes morphological reconstruction and stabilizes the lamellar structure.

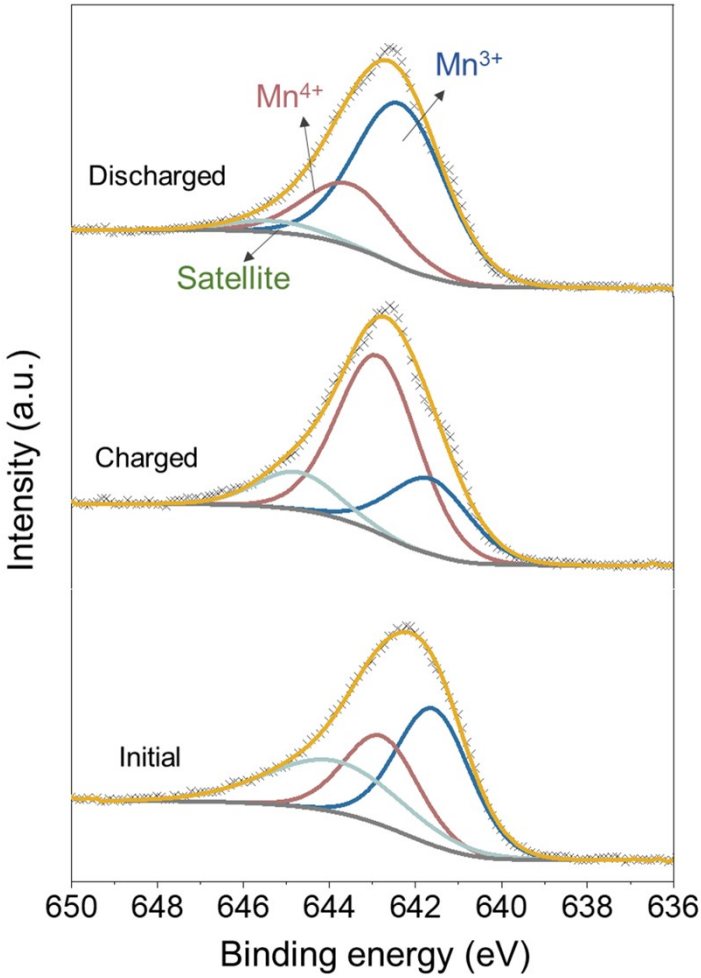

Figure S23 Ex-situ high-resolution XPS spectra of the Mn 2p region for the MnO_2 cathode at different states of charge (pristine, fully discharged, and fully charged).

The spectra reveal a reversible evolution of the manganese valence state. Upon discharge (Na^+ insertion), the Mn peaks shift to lower binding energy, indicating the reduction of Mn^{4+} to Mn^{3+}. Upon charge (Na^+ extraction), the peaks recover to higher binding energy. These results corroborate the proposed Na^+ ions intercalation/deintercalation mechanism involving the Mn^{3+}/Mn^{4+} redox couple.

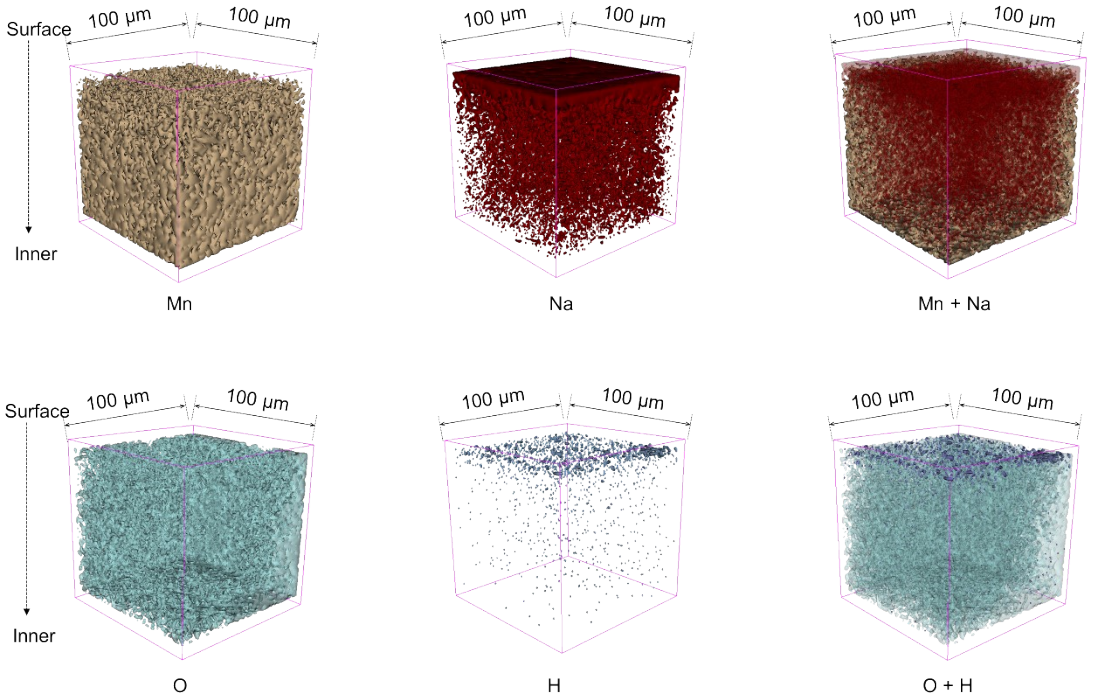

Figure S24 The 3D reconstructions of the species signal distribution in discharged MnO_2 cathode. H^- ions were only concentrated on the surface of the cathode. In comparison, the Na^+ ions distributed throughout the investigation depth, and coincides with the signal of Mn^+ and O^- fragments, implying that Na^+ ions are charge carriers in MnO_2 cathode materials.

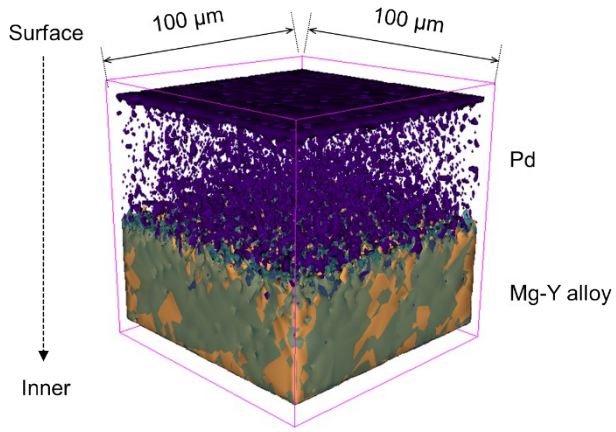

Figure S25 The 3D reconstructions of the species signal distribution in pristine anode. The Pd thin film is capped onto the Mg-Y alloy layer. Pd (purple), Mg (green), Y (orange).

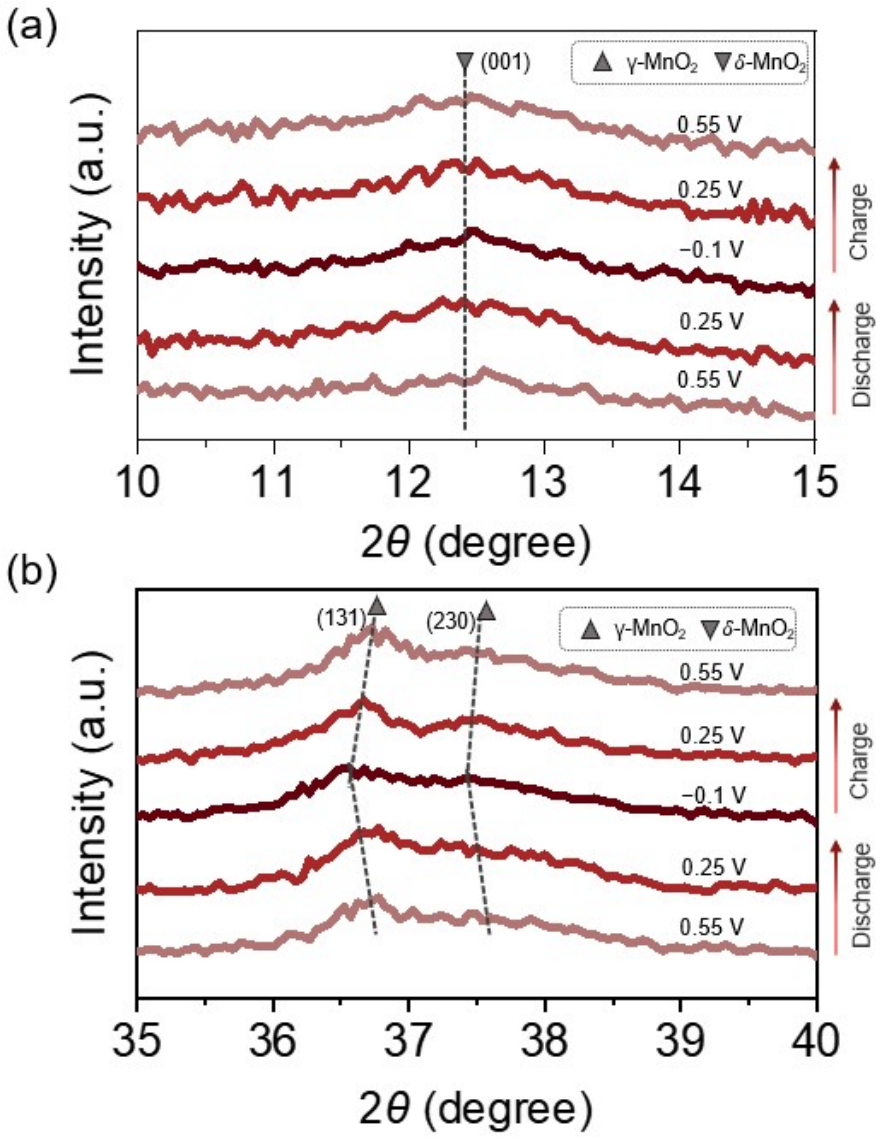

Figure S26 Partially enlarged images of the XRD patterns. (a) Ex-situ XRD patterns of (002) plane of δ-MnO_2 phase at varied discharge/charge states. (b) Ex-situ XRD patterns of (131) and (230) plane of γ-MnO_2 phase at varied discharge/charge states. The diffraction peak around 12.5°, corresponding to lamellar structure with interlayer distance of ~7.1 Å in δ-MnO_2, shows nearly no position change during the entire Na^+ ion insertion and extraction processes, indicating that the interlamellar spacing was maintained, which is primarily due to the pillar effect of intercalation of large-sized TMA^+ ions. The peaks belonging to γ-MnO_2 phase slightly shift to lower angles during discharging and return to higher angles during charging, suggesting that the γ-MnO_2 phase undergoes slight lattice expansion during Na^+ ion insertion and reversible lattice shrinkage on Na^+ ion extraction.

Table S1 | Closed-circuit mechanism of H^-–Na^+ ARDIB.

Charge		
Component	**Process**	**Charge balance**
External circuit	e^- flows from cathode → external circuit → anode	Completes electrical circuit
Cathode	$Na_xMnO_2 \overset{Charge}{\rightarrow} Na_{x-\delta}MnO_2 + \delta Na^+ + \delta e^-$	Releases Na^+ and e^-
Anode	$Mg-Y + \delta H_2O + \delta e^- \overset{\substack{Charge \\ Pd\ catalyst}}{\rightarrow} Mg-Y-H_\delta + \delta OH^-$	Consumes e^-; releases OH^-
Electrolyte	Na^+ migrates toward anode OH^- migrates toward cathode	Neutralizes electrode charge states
Discharge		
Component	**Process**	**Charge balance**
External circuit	e^- flows from anode → external circuit → cathode	Delivers energy to load
Anode	$Mg-Y-H_\delta + \delta OH^- \overset{\substack{Discharge \\ Pd\ catalyst}}{\rightarrow} Mg-Y + \delta H_2O + \delta e^-$	Releases e^-; consumes OH^-
Cathode	$Na_{x-\delta}MnO_2 + \delta Na^+ + \delta e^- \overset{Discharge}{\rightarrow} Na_xMnO_2$	Consumes Na^+ and e^-
Electrolyte	Na^+ migrates toward cathode OH^- migrates toward anode	Neutralizes electrode charge states

Table S2 | Energy densities and power densities of different micro-battery systems and our full cell at various current densities.

Electrode material (cathode// anode)	Carrier	Electrolyte	Energy density (mWh cm^{-2})	Power density (mW cm^{-2})	Ref.
This work	**H^-/Na^+**	**TMAOH+NaCl solution**	**0.43** **0.24** **0.21** **0.15** **0.11** **0.080**	**1** **4.5** **5.9** **8.0** **18.92** **30.81**	**This work**
$Na_3V_2(PO_4)_3$//$Na_2Ti_3O_7$	Na^+	$NaBF_4$-EMIMBF$_4$-PVDF-HFP ionogel electrolyte	0.15 0.13 0.10 0.071 0.058 0.051 0.044	0.072 0.14 0.32 0.66 0.99 1.32 1.95	[3]
CuHCF//FeHCF	Li^+	LiCl/PVA	0.0091 0.0081 0.0067 0.0057 0.0044 0.0024 0.0013 6.70E-4	0.068 0.14 0.33 0.68 1.34 3.43 6.53 13.44	[4]
MnHCF//MnOx/ErGO	Li^+	LiCl/PVA	0.0024 0.0020 0.0019 0.0018 0.0016 0.0015	0.050 0.097 0.15 0.19 0.257 0.49	[5]
$LiFePO_4$ // $Li_4Ti_5O_{12}$	Li^+	LiTFSI-P_{14}TFSI-PVDF-HFP ionogel electrolyte	0.15 0.12 0.099 0.082 0.072 0.054 0.040 0.019	0.035 0.071 0.10 0.13 0.11 0.25 0.30 0.43	[6]
MXene-TiS_2//MWCNTs-VO_2(B)	Zn^{2+}	$ZnSO_4$-PAM hydrogel electrolyte	0.033 0.026 0.022 0.019	0.23 0.43 0.60 0.80	[7]

			0.017 0.016	1.00 1.17	
Active carbon//Zn	Zn^{2+}	$ZnSO_4$ solution	0.12 0.11 0.11 0.10 0.087	0.40 0.80 0.16 1.58 3.89	[8]
CNT//Zn	Zn^{2+}	$ZnSO_4$ gel electrolyte	0.030 0.027 0.026 0.025 0.024 0.023	0.80 1.58 2.4 3.14 3.92 7.86	[9]
PANI//Zn	Zn^{2+}	$ZnCl_2$/PVA	0.22 0.20 0.18 0.17 0.13	0.21 0.41 0.61 0.85 1.04	[10]
MnO_2//Zn	Zn^{2+}	$ZnCl_2$-$MnSO_4$/PVA	0.16 0.14 0.11 0.075 0.047	0.18 0.46 0.95 1.78 4.49	[11]

Table S3 | Performance comparison between the H^-–Na^+ ARDIB and traditional reverse dual-ion batteries (RDIBs).

Electrolyte	Anodic carrier/ Anode material	Anode capacity	Cathodic carrier/ Cathode material	Cathode capacity	Medium voltage (V)	Ref.
30 m $ZnCl_2$	$ZnCl_4^{2-}$/ferrocene	144 mAh g^{-1}	$Zn^{2+}/Zn_3[Fe(CN)_6]_2$	65 mAh g^{-1}	0.9	[12]
1 M KOH	OH^-/VN	251 mF cm^{-2}	$K^+/K_xMn_8O_{16}$	824 mF cm^{-2}	0.9	[13]
10 m $ZnCl_2$	$ZnCl_4^{2-}$/ferrocene	35 mAh g^{-1}	$Zn^{2+}/Zn_3[Fe(CN)_6]_2$	67 mAh g^{-1}	0.9	[14]
0.8 M NaF	F^-/BiF_3	–	$Na^+/Na_{0.44}MnO_2$	137 mAh g^{-1}	0.8	[15]
1 M NaCl	Cl^-/Polypyrrole	67 mAh g^{-1}	$Na^+/Na_{0.44}MnO_2$	–	0.8	[16]
3 M NaCl+4.5 M TMAOH	H^-/Pd-capped Mg-Y alloys	1185 mAh g^{-1}	Na^+/γ-MnO_2	118 mAh g^{-1}	1.0	This work

References

[1] C. Wang, Y. Zeng, X. Xiao, S. Wu, G. Zhong, K. Xu, Z. Wei, W. Su, X. Lu, *J. Energy Chem.* 2020, **43**, 182.

[2] J. Wang, J.-G. Wang, H. Liu, Z. You, Z. Li, F. Kang, B. Wei, *Adv. Funct. Mater.* 2021, **31**, 2007397.

[3] S. Zheng, H. Huang, Y. Dong, S. Wang, F. Zhou, J. Qin, C. Sun, Y. Yu, Z.-S. Wu, X. Bao, *Energy Environ. Sci.* 2020, **13**, 821.

[4] Y. He, P. Zhang, M. Wang, F. Wang, D. Tan, Y. Li, X. Zhuang, F. Zhang, X. Feng, *Mater. Horiz.* 2019, **6**, 1041.

[5] J. Liang, B. Tian, S. Li, C. Jiang, W. Wu, *Adv. Energy Mater.* 2020, **10**, 2000022.

[6] S. Zheng, H. Wang, P. Das, Y. Zhang, Y. Cao, J. Ma, S. Liu, Z.-S. Wu, *Adv. Mater.* 2021, **33**, 2005449.

[7] B. Zhao, S. Wang, Q. Yu, Q. Wang, M. Wang, T. Ni, L. Ruan, W. Zeng, *J. Power Sources.* 2021, **504**, 230076.

[8] P. Zhang, Y. Li, G. Wang, F. Wang, S. Yang, F. Zhu, X. Zhuang, O. G. Schmidt, X. Feng, *Adv. Mater.* 2019, **31**, 1806005.

[9] G. Sun, H. Yang, G. Zhang, J. Gao, X. Jin, Y. Zhao, L. Jiang, L. Qu, *Energy Environ. Sci.* 2018, **11**, 3367.

[10] R. Li, L. Li, R. Jia, K. Jiang, G. Shen, D. Chen, *Small Methods* 2020, **4**, 2000363.

[11] H. Wang, R. Guo, H. Li, J. Wang, C. Du, X. Wang, Z. Zheng, *Chem. Eng. J.* 2022, **429**, 132196.

[12] X. Wu, Y. Xu, C. Zhang, D. P. Leonard, A. Markir, J. Lu and X. Ji, *J. Am. Chem. Soc.*, 2019, **141**, 6338-6344.

[13] C. L. Shi, J. L. Sun, F. Q. Ji, W. J. Chen, Y. Y. Pang and B. T. Liu, *Iscience*, 2022, **25**, 104141.

[14] A. Sethi, A. Kumar U and V. M. Dhavale, *ChemPhysChem*, 2023, **24**, e202300098.

[15] Z. Zhang, X. Hu, Y. Zhou, S. Wang, L. Yao, H. Pan, C.-Y. Su, F. Chen and X. Hou, *J. Mater. Chem. A*, 2018, **6**, 8244-8250.

[16] H. Kong, M. Yang, Y. Miao and X. Zhao, *Energy Technology*, 2019, **7**, 1900835.